Deb Burman, Pramit Kumar; Prabha, Thara V.; Morrison, Ross; Karipot, Anandakumar. 2018. **A case study of turbulence in the nocturnal boundary layer during the Indian summer monsoon.**

This is a post-peer-review, pre-copyedit version of an article published in *Boundary-Layer Meteorology*, 169 (1). 115-138. The final authenticated version is available online at: https://doi.org/10.1007/s10546-018-0364-4.

A CASE STUDY OF TURBULENCE IN THE NOCTURNAL BOUNDARY LAYER DURING THE INDIAN SUMMER MONSOON

Pramit Kumar Deb Burman · Thara V. Prabha · Ross Morrison · Anandakumar Karipot

Received: date / Accepted: date

Abstract Observations from the Cloud-Aerosol Interaction and Precipitation Enhancement Experiment-Integrated Ground Observation Campaign (CAIPEEX-IGOC) provide a rare opportunity to investigate nocturnal atmospheric surface-layer processes and surface-layer turbulent characteristics associated with the low-level jet (LLJ). Here, an observational case study of

---

Pramit Kumar Deb Burman
Centre for Climate Change Research
Indian Institute of Tropical Meteorology
Pune - 411008
India
E-mail: pramit.cat@tropmet.res.in

Thara V. Prabha
Cloud Aerosol Interaction and Precipitation Enhancement Experiment
Indian Institute of Tropical Meteorology
Pune - 411008
India

Ross Morrison
Land Surface Flux Measurements
NERC Centre for Ecology and Hydrology
Wallingford
Oxfordshire
OX10 8BB
United Kingdom

Anandakumar Karipot
Department of Atmospheric and Space Sciences
Savitribai Phule Pune University
Pune - 411007
India

the nocturnal boundary layer is presented during the peak monsoon season over Peninsular India using data collected over a single night representative of the synoptic conditions of the Indian summer monsoon. Datasets based on Doppler lidar and eddy-covariance are used for this purpose. The LLJ is found to generate nocturnal turbulence by introducing mechanical shear at higher levels within the boundary layer. Sporadic and intermittent turbulent events observed during this period are closely associated with large eddies at the scale of the height of the jet nose. Flux densities in the stable boundary layer are observed to become non-local under the influence of the LLJ. Different turbulence regimes are identified, along with transitions between turbulent periods and intermittency. Wavelet analysis is used to elucidate the presence of large-scale eddies and associated intermittency during nocturnal periods in the surface layer. Although the LLJ is a regional-scale phenomenon it has far reaching consequences with regard to surface-atmosphere exchange processes.

Keywords Cospectral analysis · Intermittency · Low-level jet · Nocturnal boundary layer · Wavelet analysis

1 Introduction

The atmospheric boundary layer (ABL) over land becomes thinner, less diffusive and stably stratified during typical nocturnal conditions due to the absence of surface heating and convection, and is referred to as the nocturnal boundary layer (NBL) (Stull, 1988). Generally, the NBL is considered to be stable and several studies have shown that NBL turbulence is intermittent in nature (Sun et al., 2002, 2004). The NBL has been traditionally classified into three major regimes, namely: (i) weakly stable (Malhi, 1995; Mahrt, 1998), (ii) very stable (Mahrt, 1985; Ohya et al., 1997), and (iii) intermittently turbulent (Nappo, 1991; Howell and Sun, 1999; Mahrt, 1999). Turbulent kinetic energy (TKE) in the NBL is generated solely through the action of wind shear, in contrast to the daytime convective boundary layer (CBL) where most of the TKE is associated with large-scale turbulent motions. During the evening transition over land, enhanced stability extinguishes these large-scale eddies and turbulence decays (Wyngaard, 2010).

The generation, maintenance, and decay of turbulence in the NBL is a complex interplay between a range of atmospheric phenomena including gravity waves (Fritts et al., 2003; Meillier et al., 2008; Viana et al., 2009; Durden et al., 2013; Sorbjan and Czerwinska, 2013; Wang et al., 2013), frontal activity (Mahrt, 2010; Hu et al., 2013), density currents (Blumen et al., 1999; Sun et al., 2002), shear-flow instabilities (Newsom and Banta, 2003), wave-turbulence interaction (Finnigan, 1988; Einaudi et al., 1989; Nappo et al., 2008; Román-Cascón et al., 2015) and large-scale coherent eddies (Sun, 2011; Sun et al., 2016). Such features have been investigated using theoretical methods (Frisch et al., 1978; Xue et al., 1997; Wu and Zhang, 2008a,b) and numerical simulations (Zilitinkevich et al., 2009; Zhou and Chow, 2014; Rorai et al., 2014; He and Basu, 2015). Several authors have reported intermittency as an intrinsic feature of the NBL (Chimonas, 1993; Katul et al., 1994; Coulter and Doran, 2002; Sun et al., 2002; Acevedo and Fitzjarrald, 2003; Sun et al., 2004; Mahrt, 2014), although intermittency currently lacks a cohesive definition and is often identified from the vertical velocity field.

The wind field in the NBL often has a complex structure and can be difficult to interpret. Local topography determines the wind direction in the lowest few metres, whereas the wind speed near the surface is a function of friction, buoyancy, and entrainment. After sunset, the boundary layer becomes more stably stratified, turbulence is reduced and a near-laminar layer develops. The acceleration above this laminar layer drives a jet (Blackadar, 1957), resulting in detachment of the near-surface and overlying flows (Banta et al., 2007; Banta, 2008). Turbulent eddies become smaller in the vertical and momentum transfer takes place primarily through horizontal motion. In many cases, a low-level jet (LLJ) develops during the evening and intensifies over the course of night before dissipating rapidly with the onset of convection after sunrise (Stull, 1988; Karipot et al., 2009), the existence of the LLJ often leading to high wind shear during stable conditions. Several LLJ events over south-eastern Kansas were experimentally validated during the CASES-99 (Cooperative Atmosphere-Surface Exchange Study 1999) field campaign, which pioneered efforts to quantify the structure, evolution, and physical and dynamical characteristics of the NBL (Poulos et al., 2002).

Processes that generate turbulence in the NBL have been investigated in a number of previous studies; for example, Banta (2008) found that there appears to be a strong link between turbulence within the near-surface layer and the dynamics of the LLJ. He identified different turbulent regimes in the NBL based on the atmospheric stability and the LLJ strength. However, no previous studies have focused on nocturnal LLJs occuring during the Indian summer monsoon. Several studies carried out at different locations across the globe suggest that the LLJ generates and transports turbulence downwards to the surface layer (Mahrt, 1999; Banta et al., 2003, 2006; Sun et al., 2004; Karipot et al., 2006; Prabha et al., 2007; Bonin et al., 2015). Banta et al. (2002) suggested that regions of high wind speeds within the NBL are responsible for shear production of turbulence. In Prabha et al. (2007, 2008), time—frequency characteristics of observed episodic bursts of CO_2, TKE, and momentum when the LLJ was present indicated that eddies on the scale of the height of the jet maximum were present in the surface layer. Collectively, these studies indicate that the dynamics of surface-layer turbulence are directly linked to the LLJ.

The LLJ over the Indian region is found to occur in association with synoptic-scale monsoon circulations, especially during the south-west monsoon season as a synoptic feature with local and regional components. However, very few studies thus far have examined the LLJ in the context of the Indian summer monsoon, despite the close association with larger-scale monsoon dynamics. Bunker (1965) first reported the presence of large-scale LLJs during the monsoon over Peninsular India on the basis of aircraft observations. Subsequently, this jet was found to be predominantly westerly (Joseph and

Raman, 1966) and linked to the land—ocean thermal gradient (Krishnamurti et al., 1976). The existence of the jet has since been considered as a salient feature of the Indian summer monsoon. Findlater (1969) demonstrated that the jet stream originated to the north of the Mascarene anticyclone in the southern Indian Ocean. Grossman and Durran (1984) studied the interaction between low-level flow observed during the Indian summer monsoon and the Western Ghats mountain range to examine the possible influence of complex topography on the intensification of offshore convection. Analysis by Sivaramakrishnan et al. (1992) showed the importance of downward transport of momentum and sensible heat during the night-time under near-neutral stability. It was also shown that momentum transfer occurs in bursts, under the influence of large-scale circulations during monsoon conditions while the diurnal and seasonal variation of the monsoon LLJ has been studied by, e.g., Ardanuy (1979); Kalapureddy et al. (2007); Nair et al. (2014).

NBL turbulence associated with the Indian summer monsoon jet has not yet been quantified over the Indian Peninsula. The presence of different scales of eddies within the NBL during the Indian summer monsoon has also not been examined in a systematic manner. Moreover, to the best of our knowledge, very few, if any studies, have used time—frequency analysis of the LLJ during the Indian summer monsoon. The exchange of various energy and mass fluxes, including TKE and the fluxes of momentum, sensible heat, CO_2 and water vapour between the surface layer and the boundary layer above remain unexplored during the monsoon period. Integrated observations made during the recent Cloud-Aerosol Interaction and Precipitation Enhancement Experiment (CAIPEEX) provide a unique opportunity for investigating these associations and their temporal dynamics (Prabha et al., 2011; Kulkarni et al., 2012). Our study addresses these uncertainties through the following objectives: (i) to explore the characteristics of turbulence in the NBL during the Indian summer monsoon; and (ii) to analyze the role of the LLJ in the generation and propagation of turbulence within the NBL.

2 Observations and Data Processing

The datasets used herein are based on the Cloud-Aerosol Interaction and Precipitation Enhancement Experiment-Integrated Ground Observational Campaign (CAIPEEX-IGOC) conducted during 2011; this was an integrated observational programme established at Mahbubnagar (78°45′E, 17°4′N), approximately 85 km south-west of Hyderabad, Andhra Pradesh, India (Fig. 1). Mahbubnagar is a tropical semi-urban station located in a semi-arid environment representative of a rain-shadow region, and is situated south-east of the eastern range of the Deccan Plateau on the Indian Peninsula. The field programme comprised airborne and ground-based experimental campaigns conducted to investigate the interaction between aerosol and clouds during pre-monsoon and monsoon conditions (Prabha et al., 2011). In the airborne

Table 1 List of instruments and datasets used in the present work

Instrument	Model and manufacturer	Altitudes of measurement (m)	Variable	Temporal resolution (s)	Spatial resolution (m)	Accuracy
3-D sonic anemometer-thermometer	Wind master Pro, Gill Instruments, Lymington, UK	6	T (K), T_s (K), u (m s^{-1}), v (m s^{-1}), w (m s^{-1})	0.1	–	$<$ 1.5% r.m.s
CO_2 and H_2O infrared gas analyzers	IRGA Model: LI-7500A Open Path CO_2/H_2O analyzer, Li-COR Biosciences, Lincoln, USA	6	c (μmol m^{-3}), q (g kg^{-1})	0.1	–	within 1% and 2% of readings for CO_2 and H_2O measurements, respectively
Doppler lidar	Windcube 200 (product no. WLS200-1), LEOSPHERE, France	100 to 2000	u (m s^{-1}), v (m s^{-1}), w (m s^{-1})	300	50	0.1 m s^{-1}

campaign, an instrumented aircraft was employed to collect in-situ cloud data, while the ground-based campaign consisted of tower-based observations plus several other thermodynamic and aerosol measurements. The dataset used encompasses a 12-h period from 1800 Indian Standard Time (IST) on August 15 2011 to 0600 IST on the following day. As the duration is less than a day, the timing of the events is reported without reference to the date of the observation. Details of the instrumentation used herein are summarized in Table 1. The period selected was chosen as a representative day during which monsoon convection was active over the region. The analysis focuses on NBL processes and intermittent events with fluxes and TKE derived from a micrometeorological dataset.

2.1 Micrometeorological Tower

A 20-m micrometeorological tower was installed at the measurement site, located on the southern slopes of a low-lying mountain range oriented in the north-west to south-easterly direction, the maximum height of the mountain range does not exceed 600 m. The site was characterized by non-irrigated grassland with scattered patches of low-lying shrubs. Two eddy-covariance systems were mounted at 6 m and 16 m above the soil surface, although data from the eddy-covariance system at 16 m was not available for the study period. These systems consisted of Windmaster Pro 3-D sonic anemometers—thermometers (Gill Instruments, Lymington, UK) and LI-7500A open-path CO_2/H_2O analyzers (LI-COR Biosciences, Lincoln, USA). Only data obtained at 6 m were used and eddy-covariance sensors were sampled at 10 Hz and logged using a CR-3000 Micrologger (Campbell Scientific, Logan, Utah, USA). Ambient air temperature (T in K), sonic temperature (T_s in K), the water-vapour mixing ratio (q in g kg^{-1}), CO_2 concentration (c in μmol m^{-3}), and zonal, meridional and vertical wind velocity components (u, v and w, respectively; in m s^{-1}) were used in the analysis. Raw eddy-covariance data were despiked following Vickers and Mahrt (1997) and linearly detrended following Kaimal and Finnigan (1994). A two-dimensional coordinate rotation was used to align the coordinate frames with the mean streamlines (Kaimal and Finnigan, 1994).

2.2 Doppler Wind Lidar

A Windcube 200 scanning Doppler wind lidar (LEOSPHERE, model WLS200-1) was installed at the experimental site, operating in the near-infrared range (1.54 μm) with a pulse energy of 100 μJ, a scanning cone angle of 15° and speed, and a detection accuracy of 0.5 m s^{-1} and 1.5°, respectively. The backscattered lidar signal is stored in an array of range gates having fixed time delay, with the typical beam accumulation time being 11.8 s for all directions. At each direction step, the lidar combines the four most recent radial speeds at each height to calculate the zonal, meridional and vertical wind velocity components (u, v and w in m s^{-1}, respectively). The default threshold for the carrier-to-noise ratio (CNR) is −30 dB, and the effect of the instrument range on CNR measurement is filtered. The components u, v and w are measured at 119 different levels between 100 m and 6000 m, while the horizontal wind speed (v_h in m s^{-1}) was calculated at each level using

$$v_h = \sqrt{u^2 + v^2}. \tag{1}$$

For all scan angles, u, v and w are measured along the four cardinal directions. As the full-beam rotation takes between 40 to 50 s, the time resolution of the data is irregular and ranges between 10.5 to 12.1 s, with a mean of 11.5 s; average values are stored as 5-min means. A high frequency of missing values represents a key limitation of the Windcube 200 system. Here, vertical velocities up to an altitude of 2000 m were used. Raw lidar data were only used to examine time—height contours of the vertical velocity (w). Wavelet analysis was performed on the averaged data, since a continuous record of fixed temporal resolution is a requirement for frequency domain decomposition. More details on the Windcube 200 lidar system, including an intercomparison against radiosonde observations are reported in Ruchith et al. (2014).

2.3 Synoptic Conditions

Synoptic conditions prevailing at the time of this experiment were inferred from the ERA-Interim (European Centre for Medium-Range Weather Forecasts Re-analysis) product (http://apps.ecmwf.int/datasets/data/interim-full-daily/). The zonal and meridional velocity components at the 850-hPa level at 1200 UTC (1730 IST) on 15 August 2011 were used from this product. Grid size for the wind data is $0.25° \times 0.25°$, while more details about the ERA-Interim data can be found in Dee et al. (2011). Data visualization and analysis were carried out using the Ferret software developed by the National Oceanic and Atmospheric Administration — Pacific Marine Environmental Laboratory.

2.4 Wavelet Analysis

Wavelet analysis has widespread applications in the Earth sciences, reflecting its ability to examine the non-linear and non-stationary components of time series (Lau and Weng, 1995; Torrence and Compo, 1998). A time series can be simultaneously decomposed in a two-dimensional time–frequency domain by this method, providing unique advantages over other time-series analysis techniques, such as the frequency spectrum (Farge, 1992) or Fourier transform (Thomas and Foken, 2005). Wavelet analysis has been used previously to examine ABL turbulence and associated scalar mixing (Hudgins et al., 1993; Salmond, 2005; Terradellas et al., 2005; Woods and Smith, 2010; Zeri and Sá, 2011), and is used herein to separate the energies contained in the frequency bands of a set of turbulent time series to analyze energetic interaction among different scales of turbulent motion. Continuous wavelet analysis in the time–frequency domain (Torrence and Compo, 1998) was employed on w and v_h measured by the lidar at different altitudes, as well as for fluxes obtained using the eddy-covariance technique.

Wavelets ($\psi_0(\eta)$) are analysis functions localized in space, with the functions dilated or contracted before convolving with the signal. Continuous wavelet transform of a regularly spaced time series, x_n, with a timestep of

δt can be expressed using

$$W_n(s) = \sum_{n\prime=0}^{n-1} x_{n'} \psi^* [\frac{(n'-n)\delta t}{s}], \tag{2}$$

where, $\psi^*[(n'-n)\delta t/s]$ is the normalized complex conjugate of a scaled and translated version of $\psi_0(\eta)$. The wavelet power is defined as $|W_n(s)|^2$, and can be rewritten as $W_n(s).W_n^*(s)$, where $W_n^*(s)$ is the complex conjugate of $W_n(s)$.

The Morlet wave function was used since it has found extensive application in dealing with the stable ABL (Everson et al., 1990; Qiu et al., 1995; Thomas and Foken, 2005; Prabha et al., 2007, 2008); this wave function with an angular frequency ω_0 is defined as

$$\psi_0(\eta) = \pi^{-\frac{1}{4}} \exp(i\omega_0\eta) \exp(-\frac{\eta^2}{2}). \tag{3}$$

Scales analyzed are written as fractional powers of two and are derived from the following relations (Farge, 1992; Torrence and Compo, 1998),

$$s_j = s_0 2^{j\delta j}, j = 0, 1, 2, 3......J, \tag{4}$$

$$J = \frac{1}{\delta j} \log_2 \frac{N\delta t}{s_0}, \tag{5}$$

where s_0 and J determine the smallest and the largest resolvable temporal scales, respectively. A value of 0.5 has been used here for δj as it is the maximum value that still allows the maximum sampling rate. White noise was used as the background spectrum to check the significance of any peak appearing in $|W_n(s)|^2$.

Scale-averaged wavelet power is defined as the weighted sum of the wavelet power spectrum over the time periods in a specific band. Here, eddies have been classified into multiple scales according to their time periods and scale-averaged wavelet power for these bands was calculated and plotted in order to compare their relative contributions to the total power.

2.5 Cospectral Analysis

Cospectral analysis has particular utility for identifying the sources and sinks of scalars within the ABL (Zeri and Sá, 2011), the propagation of gravity waves (Viana et al., 2009; Sorbjan and Czerwinska, 2013) and large coherent eddies (Sun et al., 2016), as well as other coherent structures. We have investigated the genesis and transport of turbulence through different heights within the NBL using this technique.

The cross spectrum between two time series, $x_n(A)$ and $x_n(B)$ is defined as $G_{AB} = W_n^A(s).W_n^{B*}(s)$ where the cospectrum (Co) is obtained after separating the real and imaginary parts. Alternatively,

$$G_{AB} = Co - iQ, \tag{6}$$

where Q is the quadrature spectrum and Co is an alternate representation of the covariance between $x_n(A)$ and $x_n(B)$. Here, Co was calculated and plotted using different variables to explore the mutual effects of these on each other. The phase difference between these two time series is defined as

$$\phi_{AB} = \tan^{-1} \frac{Q}{Co}, \tag{7}$$

and used to differentiate the relative contributions of different phenomena (e.g. gravity waves, non-linear waves, etc.) to total boundary-layer turbulence.

3 Results and Discussions

Figure 1 shows wind vectors at the 850-hPa level at 1730 IST on 15 August 2011, with a strong westerly flow prevalent over the measurement site on this date. This is a synoptic feature of the Indian summer monsoon, and the presence of this westerly flow indicates an active Indian summer monsoon over the central Indian region during the study period. In the first part of this analysis is mostly based on the data from the Windcube 200; vertical profile analyses from this instrument form the context for the later analysis where micrometeorological tower data have been used.

Wave-like oscillations were observed in the horizontal wind speed at different altitudes during the study period, and an LLJ was also present. These oscillations become more prominent with the strengthening of the LLJ at around 0000 IST. 30-min averages of u and v calculated from the lidar data are plotted as functions of altitude in Figs. 2a and 2b, respectively, where a zone of maximum wind speed or the 'jet nose' can be seen in the wind profile (Fig. 2a). The wind speed clearly decreases both above and below this nose; such a wind profile is typical of the classic LLJ structure (Pichugina and Banta, 2010). The maximum wind speed was observed at an altitude of 400 m from 0300 to 0330 IST, representing the nose or jet core; it can be seen that the meridional velocity component was smaller than the zonal component (Fig. 2). The maximum value of $v = 4 \pm 1$ m s^{-1} (Fig. 2b), and the maximum value of $u = 11 \pm 1$ m s^{-1} (Fig. 2a) during the same time interval. Wind direction remained predominantly westerly, with the wind speed at the jet core remaining at 11.8 ± 1.3 m s^{-1} during the period of observation.

Pichugina and Banta (2010) show that for the stable boundary layer with a traditional LLJ structure having a prominent nose, as seen in our case from Fig. 2, the height of the boundary layer (h) is most accurately given by the height of the first significant minimum in the vertical profile of the variance of the horizontal wind speed (σ^2_{Vh} in m^2 s^{-2}). Following this, the vertical profile of σ^2_{Vh} was calculated from the lidar data at 10-min intervals, with several representative profiles plotted in Fig. 3 for estimating h. The first significant minimum in σ^2_{Vh} occurs at 500 m at 1900, 0100, 0200 and 0500 IST; however, minima were observed at 350 m at 2000 and 0300 IST. These two heights are marked as h_A and h_B in Fig. 3. Finally, h has been approximated as the average of h_A and h_B with an error bar of half of the difference between h_A and h_B i.e. $h \approx 425 \pm 75$ m.

Such a high horizontal wind speed at the jet core, as seen from Fig. 2, introduces strong vertical shear in the atmosphere. Vertical shear in horizontal wind speed can be obtained from the lidar data (Fig. 4), using

$$S_V = \frac{dv_h}{dz}, \tag{8}$$

where the maximum magnitude of this shear as shown in Fig. 4 is ≈ 0.05 s^{-1}.

Observations of u, v and w were obtained every 5 min from the lidar at all measurement heights, with analyses of lidar data confined to 2000 m. Hence 'all heights' are representative of all available heights up to 2000 m, unless stated otherwise. Note that v_h is calculated for all heights using Eq. 1, and standard deviations for u and v (σ_u and σ_v, respectively) are calculated from the lidar data at all heights at 30-min intervals. As the time resolution of the wind lidar data is 5 min, each 30-min record contains six measurements of u and v. The temporal mean of v_h ($\overline{v_h}$) was also calculated for each of these 30-min periods. Finally, σ_u and σ_v are normalized by $\overline{v_h}$ (σ_{uN} and σ_{vN}, respectively) at all heights for each 30-min period. These parameters ($\sigma_u/\overline{v_h}$ and $\sigma_v/\overline{v_h}$) are dimensionless and indicative of the turbulence intensity, with vertical profiles of these parameters plotted in Figs. 2c and 2d, respectively.

Mean vertical velocity ($\overline{w}$ in m s^{-1}) during the period of our study has been calculated at all vertical levels from the lidar data, with fluctuations in w (w') during this period calculated by subtracting $\overline{w}$ from w. The time–height contour plot of w' from the lidar is shown in Fig. 5, where Updrafts and downdrafts are seen to occur in an alternating fashion. However, two strong updraft events take place at 1915 and 0100 IST that are annotated by the black vertical dashed lines. The occurrence of these events coincides with the appearance of strong velocity shear (Fig. 4), whose presence is highlighted using vertical black dashed lines in Fig. 4.

3.1 Scale-averaged Variance

Five different periodicities were considered to represent large (128-256 min), coherent (64-128 min) and small (10-16 min) scales. Each of these scale-averaged variances acts as a measure of the energy associated with the eddies having time periods within each respective band (Fig. 6).

The appearance of a sharp peak was not observed for eddies in the frequency band at 128-256 min (Fig. 6), however, the maximum amount of scale-averaged variance was observed for the same eddies at around 0100 IST at the time when the LLJ is strengthening. Statistically significant peaks were simultaneously observed for eddies in the 64-128 min band, and an increase in power was also observed around 0300 IST for this band. For the 32-64 min band, peaks appeared later at around 0145 IST. Subsequent to this, eddies in the 16-32 min and 10-16 min bands record peaks at 0215 and 0330 IST, respectively. In general, peaks were observed at later times for smaller-scale events.

The maximum magnitude of the scale-averaged variance increases with decreasing time scale, and for the 128-256 min eddies it is 0.01 m^2 s^{-2}, compared to 0.06 m^2 s^{-2} for 10-16 min eddies. A six-fold increase in the magnitude of scale averaged variance was observed between the smallest and largest scales considered; for 64-128, 32-64 and 16-32 min frequency bands, maximum values were 0.02, 0.015 and 0.05 m^2 s^{-2}, correspondingly.

As scale-averaged variance represents the amount of energy contained in a particular band of frequencies (Torrence and Compo, 1998), this can be interpreted as an example of an energy cascade from larger to smaller turbulent scales (Wyngaard, 2010). Energy in the form of large-scale turbulent eddies is introduced into the atmosphere by the LLJ at levels beneath the jet nose. This energy is in turn transferred to smaller eddies in a process analogous to the redistribution of TKE within layers between the LLJ and land surface (Smedman et al., 1993).

Peaks appear in the 32-64 min eddies at all levels around 1830 IST (Fig. 6), with peaks occurring later (1930 IST) for the 16-32 min and 10-16 min eddies (Fig. 6). Increases in scale-averaged variance were observed at 2030, 2300, 0030 and 0215 IST for the 16-32 min eddies (Fig. 6) and multiple peaks were also observed for 10-16 min eddies at 2030, 2330, 0200 and 0330 IST (Fig. 6). Smaller peaks were observed for 32-64 min eddies around 0000 and 0345 IST (Fig. 6). Such small peaks were also seen to appear in 16-32 min eddies around 0030 and 0215 IST (Fig. 6). For 10-16 min eddies, peaks were observed at around 0000, 0200 and 0330 IST (Fig. 6).

The appearance of peaks containing significant energy coincides with the temporal evolution of the LLJ (Figs. 2 and 5). Strong mechanical shear produced by the LLJ was present in the atmosphere during the time of large-scale oscillations, i.e. when the 128-256 min and 64-128 min eddies were present (Fig. 5). These large eddies are generated by several means, including gentle gravity waves and/or non-linear waves, as well as passing disturbances, and subsequently decay into smaller eddies at levels below the jet core. This is illustrated by the cospectral plot for w at different levels below the jet core (Figs. 7 and 8); w at 500 m was taken as a reference for this purpose and cospectra with w at other levels are calculated. The height of this reference level was chosen to be 500 m as the LLJ maximum was close to this height during the observational period. Only two cospectra plots are presented, namely those with w at 100 m and 450 m (Figs. 7 and 8, respectively). These correspond to the levels that are closest and most distant to the 500-m reference level.

The LLJ was observed to facilitate the downward propagation of the large-scale eddies that are present in the upper level of the boundary layer. Maximum correlation was observed for the 128-256 min and 64-128 min eddies (Fig. 7). The timing of correlation for 128-256 min eddies occurred between 0030 - 0330 IST. For 64-128 min eddies the maximum correlation was observed between 2330 - 0200 IST at the time when the wind shear was strongest due to the presence of the LLJ (Fig. 4). Correlation values increase for all time scales at 450 m. For 128-256 and 64-128 min eddies, the maximum correlation occurred between 2130 - 0330 and 2330 - 0100 IST.

Wind shear is responsible for generating small scale turbulent events observed at all levels. Another, weaker, wind shear event that was not related to the LLJ was observed between 1930 and 2100 IST (Fig. 4), with the maximum correlation observed for 16-32 min eddies around this time at both 100 m and 450 m (Figs. 7 and 8 respectively). This implies that smaller-scale temporal events at all levels coincide with the periods of increased wind shear. As outlined above, wind shear transports large-scale eddies from upper levels downwards, and in turn, these large-scale eddies generate smaller-scale processes in the surface layer. This also implies the presence of large-scale as well as small-scale features in the lower atmosphere.

3.2 Surface Fluxes and TKE

The vertical velocity w measured by the sonic anemometer at 6 m is shown in Fig. 9a. Vertical kinematic fluxes of TKE ($\overline{w'e'}$ in m^3 s^{-3} where e is TKE) and sensible heat H ($\overline{\theta' w'}$ in K m s^{-1}) are presented in Fig. 9b, with the magnitude of H fluctuating around zero during this period. This is characteristic of the lack of buoyant production of turbulence during the nocturnal period. Radiative cooling of the surface takes place, together with the cooling of the atmospheric surface layer, which is supported by the observed negative values of H (Karipot et al., 2008).

Turbulence was not completely absent in the surface layer as is evident from the non-zero values of $\overline{w'e'}$. During most of the time, $\overline{w'e'}$ remained of negligible magnitude and negative. Several occurrences of large negative peaks in $\overline{w'e'}$ were observed over the study period; the first of these was observed around 1900 IST when $\overline{w'e'} = -0.02$ m^3 s^{-3}; additionally, $\overline{w'e'}$ $= -0.06$ m^3 s^{-3} around 2030 IST, with $\overline{w'e'}$ remaining close to zero until 2200 IST. A sharp fall in its value was observed at 0000 IST when it became slightly lower than -0.07 m^3 s^{-3} before remaining close to zero for the remainder of the night. The sensible heat flux was lowest at 1900 IST. The magnitude of this negative peak is -0.003 K m s^{-1}, coinciding with the negative peak in $\overline{w'e'}$. Another broad negative peak in H is observed during 2000 to 2030 IST, and closely coincides with the negative peak in $\overline{w'e'}$ at 2030 IST. Non-exact coincidence of the sensible heat and TKE fluxes in time may occur if counter-gradient fluxes are present (Lee et al., 1996; Prabha et al., 2007).

Vertical kinematic fluxes of u and v ($\overline{u'w'}$ and $\overline{v'w'}$, respectively, in m^2 s^{-2}) were also calculated for each 30 min from the eddy-covariance data at 6 m (Fig. 10a). The sum of both these zonal and meridional momentum fluxes ($\overline{u'w'}$ + $\overline{v'w'}$) is also shown. Both of these momentum fluxes showed a significant increase in magnitude around 1930 IST, with absolute values for both of these fluxes comparable and close to 0.10 m^2 s^{-2}. Additionally, another peak was observed in zonal momentum flux around 2030 IST, with peaks also observed around 2300, 0000, and 0010 IST. The sum of the zonal and meridional momentum fluxes registers positive peaks at 2030, 2300, 0000 and 0100 IST. The maximum magnitude for these peaks was 0.10 m^2 s^{-2} at 2030 IST followed by $\approx$ 0.08 m^2 s^{-2} at 0000 IST.

Vertical kinematic fluxes of the zonal and the meridional wind velocity components ($\overline{u'w'}$ and $\overline{v'w'}$, respectively) registered large positive peaks at around 1930 IST, and coincide with the occurrence of a local but strong velocity shear. Subsequently, at around 0000 IST, positive and negative peaks were observed in $\overline{u'w'}$ and $\overline{v'w'}$, correspondingly. appearing at around the same time when very strong vertical velocity shear is generated by the development of the LLJ (Fig. 4). These peaks imply a significant amount of momentum exchange between the surface and the levels above. Hicks et al. (2015) recently illustrated downwards transfer of momentum associated with a downburst resulting in a periodic increase in wind speed at ground level, attributing this to the synoptic-scale events rather than to surface characteristics. In our study, however, both upwards and downwards transfer of momentum occur simultaneously with strong updrafts, strengthening the proposition that momentum transfer takes place in association with the velocity shear in the atmosphere. Moreover, the LLJ appears to drive the transfer process, as is evident from the cospectral analyses presented previously (Figs. 7 and 8; Sec 3.1). This represents a classic example of the top-down nature of the turbulence that exists in the presence of vertical shear and in the absence of convection (Banta et al., 2003; Mahrt, 2014).

3.3 CO_2 and Water Vapour Fluxes

Vertical kinematic fluxes $\overline{q'w'}$ (in g m kg^{-1} s^{-1}) and $\overline{c'w'}$ (in μmol m^{-2} s^{-1}) were calculated from the eddy-covariance data at 6 m (Fig. 10b); $\overline{c'w'}$ remains positive for the entire duration of the observation period, except at 2200 IST when it decreased to zero. Positive peaks appear in $\overline{c'w'}$ at 1900 and 0000 IST (Fig. 10b) with magnitudes of 0.28 μmol m^{-2} s^{-1} and 0.18 μmol m^{-2} s^{-1}, respectively. Similarly, $\overline{q'w'}$ remained positive during the entire period with positive peaks at 1930 (0.025 g m kg^{-1} s^{-1}) and 0000 IST (0.015 g m kg^{-1} s^{-1}). It is evident that the peaks in fluxes of momentum, sensible heat and TKE, as well as CO_2 and water vapour, appear around the time when non-zero vertical shear was observed in association with the LLJ (Fig. 4).

Peaks appearing in the vertical kinematic fluxes of CO_2 and moisture around 1930 IST (Fig. 10b) coincide with local shear. Another set of peaks appear simultaneously in both these fluxes around 0000 IST (Fig. 10b), again coinciding with velocity shear related to the LLJ. Hence, mechanical shear is seen to play an important role in vertical exchanges of moisture as well as CO_2 between the surface and atmospheric levels above, enhancing the upward transport of water vapour and CO_2. During the nocturnal period, production of these two variables is considered to be dominated by the respiration processes of plants and the soil, while, turbulent fluxes are thought to be closely correlated with the friction velocity (u_*) (Aubinet et al., 2012). Hence, fluxes appearing at nighttime during low u_* conditions are commonly treated as errors and filtered out. However, several authors have pointed out the limitations of this approach as it seriously underestimates the pollutant and water vapour fluxes at night-time that arise as a result of shear-induced turbulence (Salmond et al., 2005; Prabha et al., 2008). A slightly different mechanism associated with the passage of a cold front simulated by Hu et al. (2013), also illustrates the importance of strong mechanical shear, resulting in intermittent bursts of turbulence and the negative counter-gradient fluxes of sensible heat as reported in the present study. A gravity wave event was seen to generate significant amount of CO_2 and sensible heat fluxes under low u_* conditions (Zeri and Sá, 2011), although, in their study, the CO_2 flux was negative since the gravity wave carried CO_2-rich air downwards, in contrast to the results presented here. The present study clearly indicates that mechanical shear acts as a driving mechanism for fluxes in the NBL, which is otherwise treated as stably stratified and weak in terms of turbulent mixing. It also emphasizes the importance of understanding the dynamics of night-time fluxes in order to improve currently accepted nocturnal data-filtering techniques (Gu et al., 2005).

3.4 Intermittency

The data presented for TKE and other fluxes suggest a downward transfer of TKE with associated changes in the surface fluxes (Fig. 10), that coincide with the occurrence of the LLJ. The presence of the intermittency is evident in vertical velocity measured using the eddy-covariance technique (Fig. 9a), with two clear events at 1915 and 2300 IST (Fig. 11). The scale-averaged variance for 128-256 min eddies was very low and insignificant, being lower than the white-noise threshold. Two broader insignificant peaks were observed for 64 to 128 min eddies at around 2100 and 0100 IST, while three broader and significant peaks were observed for 32-64 min eddies. These were of comparable magnitude to one another (around 1×10^{-4} m^2 s^{-2}), appearing at around 2045, 0015 and 0245 IST. For 16-32 min eddies, multiple, sharper peaks evolved at 1945, 2045, 0000, 0030, 0215 and 0315 IST, with the largest peak observed at 2045 IST, with a magnitude of approximately 6×10^{-4} m^2 s^{-2}. In this case, the magnitude of the scale-averaged variance was proportional to the decreasing time scale of the eddies. There was a six-fold increase in absolute values of the scale-averaged variance between the largest (64-128 min) and smallest (10-16 min) eddies considered.

Velocity shear in the atmosphere introduces turbulent eddies in the surface layer (monitored at 6 m). As seen from observations discussed above, local velocity shear around 1900 IST resulted in an increase in the power contained within the 64-128, 32-64 and 16-32 min eddies in w. However, the increase in power for 64-128 min eddies was not statistically significant, suggesting that generation aloft and the downward propagation of turbulence is responsible for the genesis of these high-frequency events.

The cross-spectrum between T and w at 6 m was calculated from eddy-covariance data. The phase difference (ϕ_{wT}) of 90° between w and T (Fig. 12) can be attributed to gravity waves (Stull, 1988; Lee et al., 1996; Nappo, 2012), whereas for events having larger time scales a phase difference of 180° between w and T is possibly due to non-linear waves. Additionally, for turbulent events, a phase difference of 180° between w and T is expected at smaller time scales (Barthlott et al., 2007; Prabha et al., 2007).

ϕ_{wT} has a wide range of variation between 0° and 160° for events with time scales of 256-512 min (Fig. 12), and for these events ϕ_{wT} remained close to 20° between 1830 - 2300 IST, and close to 90° between 0400 to 0600 IST. ϕ_{wT} fluctuated randomly between 0° to 160° for 128-256 min events, and there are several instances when it attained a value close to 90°. Similarly, ϕ_{wT} is equal to 90° at multiple times for the 64-128 min events, for example, ϕ_{wT} approaches a value of 90° during 2000 - 2300 IST and 0130 - 0330 IST for both 64-128 and 32-64 min events, and alternated rapidly between 20° and 180° for events with time-periods of less than 32 min. Hence, certain contributions from gravity waves and non-linear waves are seen in large-scale eddies, i.e. 128-256, 64-128 and 32-64 min oscillations. At small scales, these waves are dominated by turbulence.

Scale-averaged variances were also calculated for the horizontal velocity component from sonic anemometer data (Fig. 13). Figure 13 shows that 128-256 min eddies do not show any significant peaks throughout the observation period, although, significant peaks were observed for 64-128, 32-64 and 16-32 min eddies. For 64-128 min eddies, multiple peaks of a broader nature were observed, with one such peak observed around 0030 IST, with a magnitude of $\approx 5 \times 10^{-4}$ m^2 s^{-2}. Multiple peaks were observed in 32-64 min eddies at approximately at 2345, 0115 and 0400 IST; the first of these peaks had a maximum value of approximately 0.01 m^2 s^{-2}. For 16-32 min eddies, three broader peaks were observed at approximately at 0000, 0045 and 0415 IST. The first of these had a maximum value of 0.05 m^2 s^{-2}. As observed for earlier cases, the variance increases with the decreasing time scale of eddies (Fig. 6). However, the increment in absolute values of scale-averaged variance between the largest (64-128 min) and smallest (10-16 min) eddies was more than two orders of magnitude (400) larger. This increment is much larger compared to that of w (Fig. 11).

Scale-averaged variances were calculated for a 30-min time series of w measured at 6 m with the eddy-covariance sensors from 1930 IST onwards. Two separate time were considered in order to differentiate contributions from smaller and larger scales of eddies to the total turbulence. Eddies with time

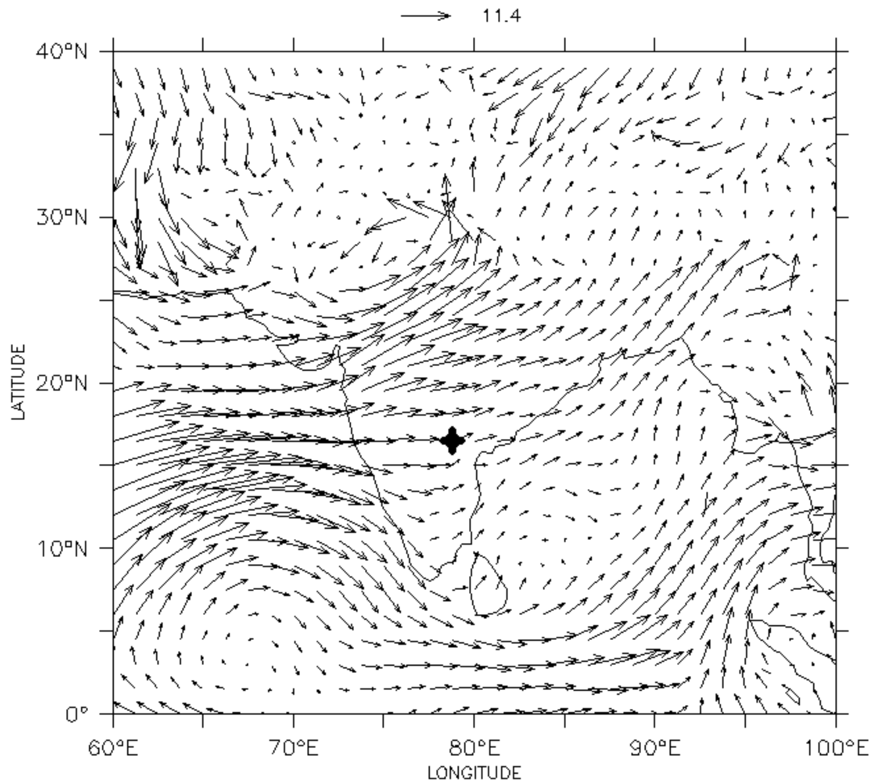

Fig. 1 Geographical distributions of 850-hPa wind vectors (m s^{-1}) over the Indian region at 1730 IST on 15 August 2011. The arrow on top of the figure denotes the scale of the vector. The location of the measurement site is marked by a black star. Data are from the ERA-Interim dataset.

periods in the range from 0.0033 to 15 min and 15 to 30 min are clustered together as 'turbulent' and as 'non-turbulent', respectively (Fig. 14).

4 Discussion

Turbulence in the atmosphere during our study period can largely be attributed to mechanical shear since the thermal production of turbulence is absent. Negative peaks in $\overline{w'e'}$ are observed frequently implying the downward transport of turbulence (Mahrt, 1999; Banta et al., 2002). This process has been suggested by Mahrt and Vickers (2002) as one of the criteria for detecting cases when turbulence generated at the upper levels is transported downwards. The occurrence of each of these peaks coincides with the generation of strong vertical shear in the horizontal velocity. During the period 1915 - 2100 IST a local velocity shear is observed up to an altitude

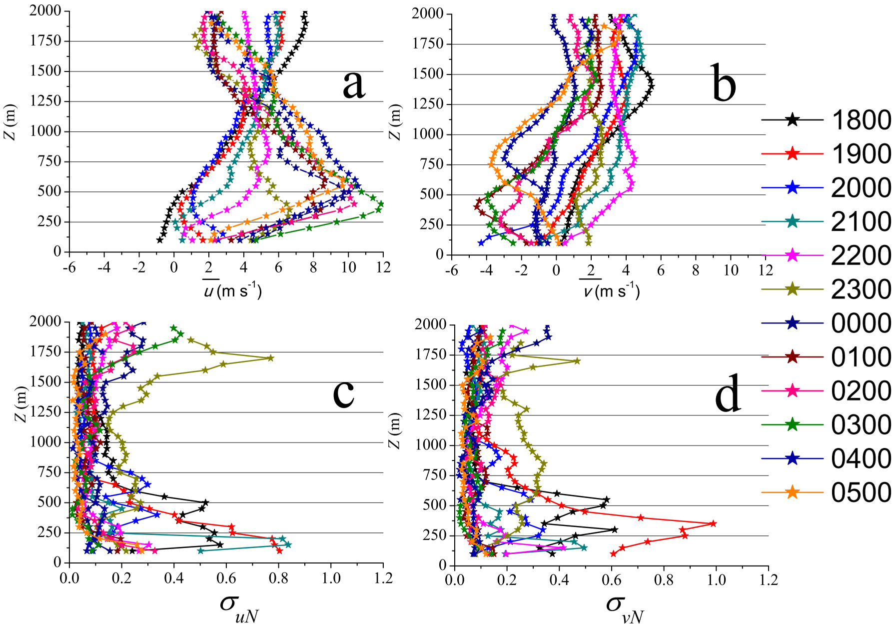

Fig. 2 Vertical variation of 30-min averages of (a) zonal velocity component (u) and (b) meridional wind component (v); and the vertical distributions of (c) standard deviation of zonal velocity component (σ_{uN}; dimensionless) and (d) standard deviation of meridional velocity component (σ_{vN}; dimensionless) calculated for 30-min period at hourly interval and normalized by mean horizontal wind speed. The legend shows the corresponding times in IST. Data are from the Windcube 200 lidar up to 2000 m.

of 300 m, resulting in a highly negative $\overline{w'e'}$. The appearance of the second peak coincides with the development of the LLJ that starts strengthening around 0000 IST and results in strong velocity shear at all levels below the jet nose. At around this time, a second negative peak was observed in $\overline{w'e'}$, and interestingly, this peak was more negative than the first. It can be thought of as an outcome of the stronger shear induced by the LLJ. These results support those of Duarte et al. (2015), where turbulence in the NBL was found out to be more prominent on days with the occurrence of the LLJ, since higher wind speeds lead to more intense turbulence in the NBL. Mechanical production of TKE possibly occurs below the jet core (Smedman et al., 1993). The maximum wind speed is observed at this height, and as a result maximum shear is observed between this level and adjacent levels. TKE is transported away by pressure transport to the layers above and below the LLJ (Smedman et al., 1993; Berström and Smedman, 1995; Cuxart et al., 2002). However, transport of TKE above the level of the LLJ remains restricted to within a thin atmospheric layer (Smedman et al., 1993). The results of the cospectral analysis also support this hypothesis, as significant power was observed to

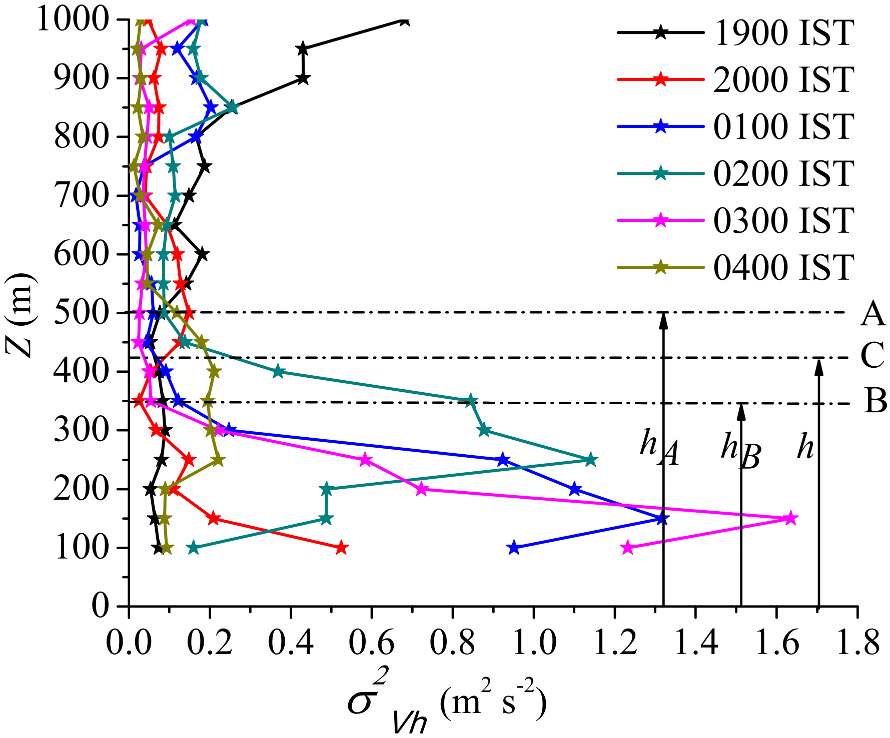

Fig. 3 Vertical profiles of the variance of horizontal wind speed (σ^2_{Vh}) calculated for 10-min periods. Figure legend represents the corresponding times in IST. The horizontal dashed lines in black, A and B mark the heights h_A and h_B respectively. These are the heights at which the first significant minimum values in σ^2_{Vh} are observed at different times. The average height of the boundary layer (h) during the period of our study is approximated to be the average of h_A and h_B and marked by the horizontal black dashed line C. h_A, h_B and h are marked by the vertical arrows. Data are from the Windcube 200 lidar up to 1000 m.

be concentrated in 128-256 min and 64-128 min eddies around these times. The LLJ starts weakening after around 0400 IST, and this is reflected in the cospectral analysis as powers concentrated in these eddies start reducing.

Variances of the zonal and the meridional velocity components normalized by the mean horizontal wind speed provide qualitative estimates of the mechanical turbulence (Prabha et al., 2007). Normalizing the variance in this way neutralizes any effect that might significantly change the mean value, making it more suitable for inter-comparisons. Figures 2c and 2d show that this parameter for u and v has significant variations in the lowest 500 m of the ABL under the influence of the LLJ. At upper levels, different profiles calculated in the same way merge with each other and are characterized by very small values. Fluctuations observed around this value are also significantly lower compared to the lowest 500 m of the boundary layer. These observations suggest the presence of two distinct turbulent zones above and

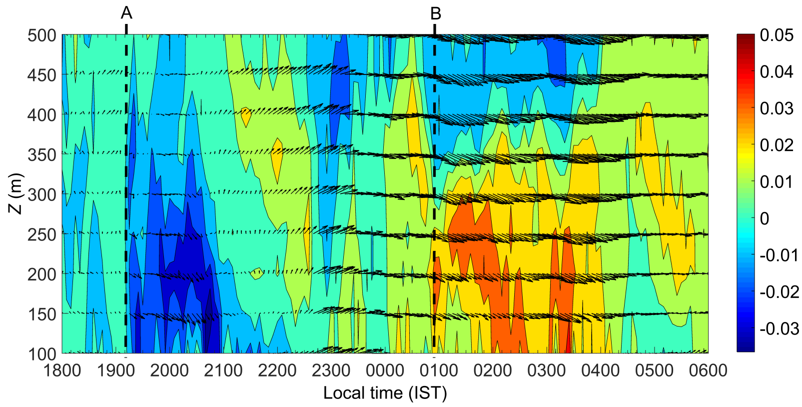

Fig. 4 Time-height contour plot of the vertical shear in the horizontal wind speed (S_V in s^{-1}) below the low-level jet. The arrows are indicative of wind speed (length of arrows) and direction. The colour bar shows the scale in s^{-1}. Two strong occurrences of the shear are marked by the vertical black dashed lines A and B which are seen to take place around 1915 IST and 0100 IST, respectively. Data are from the Windcube 200 lidar up to 500 m.

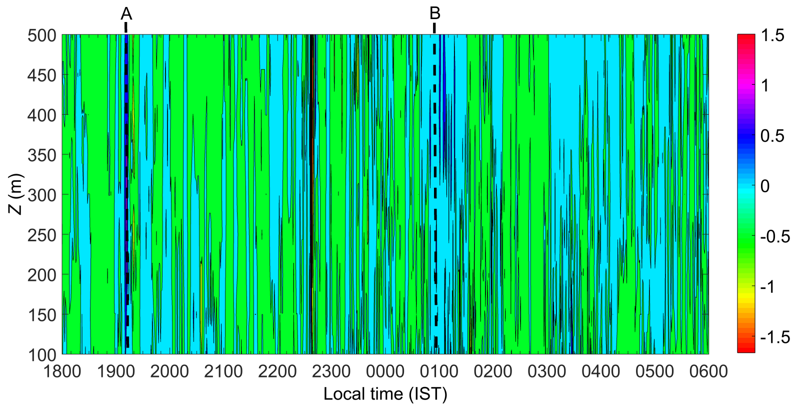

Fig. 5 Time-height contour plot of the fluctuations in vertical velocity (w' in m s^{-1}) below the low-level jet. w' is calculated by subtracting the mean w ($\overline{w}$) during the 12-h period from 1800 IST on August 15 2011 to 0600 IST on the following day from w at each vertical level. The colour bar shows the scale in m s^{-1}. Two strong updrafts are seen around 1915 IST and 0100 IST which are marked by the vertical black dashed lines A and B which, respectively. Data are from the Windcube 200 lidar.

below the LLJ. Layers above the LLJ are less turbulent whereas those layers below the jet are more turbulent and better-mixed. This is supported by the results of Smedman et al. (1993) who concluded that the confinement of mechanically-generated turbulence to within a thin layer above the LLJ resulted in a well-defined maximum. It also suggests that turbulence is carried downwards from the level of production to enhance the turbulence in the layers below. Beyond an altitude of 1500 m, normalized velocity variances show significant fluctuations at specific times; however, detailed analysis of

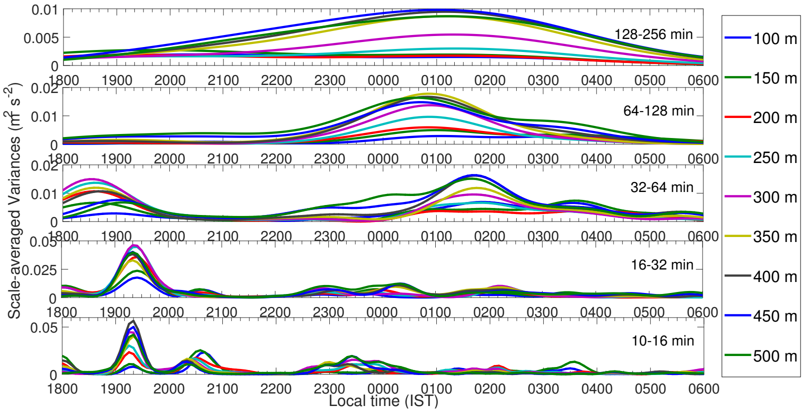

Fig. 6 Scale-averaged variances of vertical velocity (w) contained in different frequency-bands at multiple heights above the land surface. Different colours in each panel correspond to different heights. The y-axis scale differs from panel to panel. Data are from the Windcube 200 lidar up to 500 m.

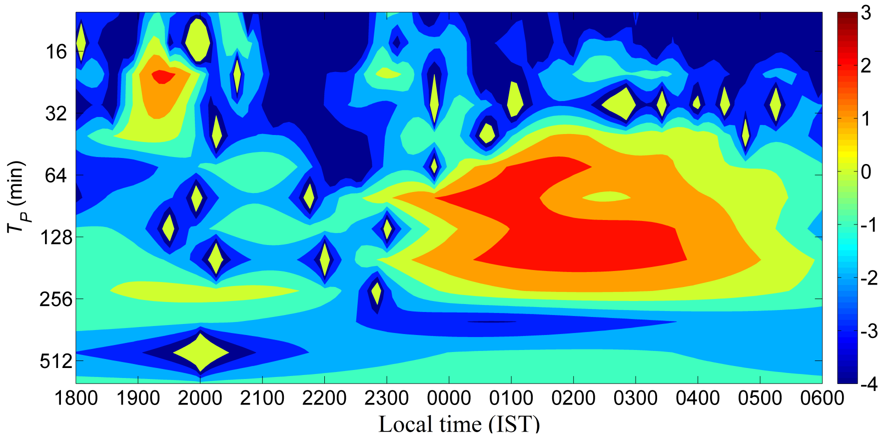

Fig. 7 Cospectrum (Co) between vertical velocity (w) at 100 m and 500 m. The x and y axes show the time of occurrence (IST) and the time period (T_P in min) of the oscillations, respectively. The scale on the y-axis is in reverse order. The colour bar shows the scale in m^2 s^{-2}. Data are from the Windcube 200 lidar.

these fluctuations remains beyond the scope and objectives of the present study.

Based on the arguments presented above, the genesis of nocturnal turbulence can be attributed principally to mechanical shear. The turbulence is generated aloft, and subsequently transported downwards. It can also be thought of in terms of as being introduced in the form of the larger turbulent motions, which gradually decay into smaller eddies. Thus, the turbulent energy is transferred from the height of the jet height to smaller turbulent scales.

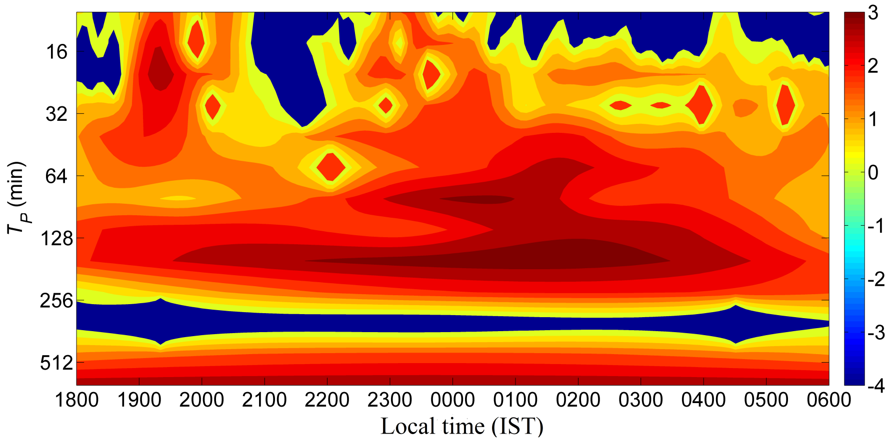

Fig. 8 Cospectrum (Co) between vertical wind velocity (w) at 450 m and 500 m. The x and y axes show the time of occurrence (IST) and the time period (T_P in min) of the oscillations, respectively. The scale on the y-axis is in reverse order. The colour bar shows the scale in m^2 s^{-2}. Data are from the Windcube 200 lidar.

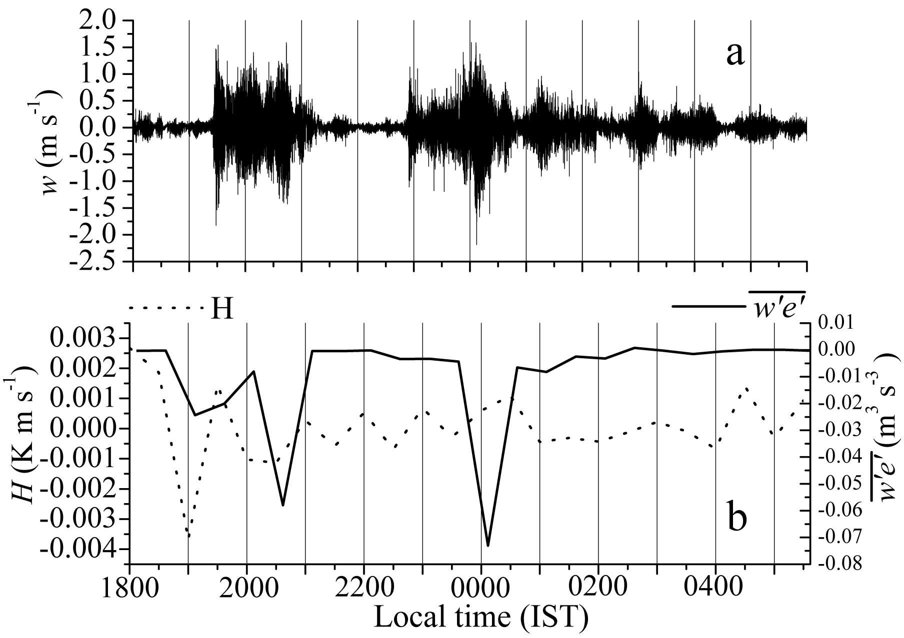

Fig. 9 Temporal variations of (a) fluctuation in vertical wind velocity (w) and (b) vertical kinematic fluxes of TKE ($\overline{w'e'}$) and sensible heat (H) calculated using the eddy-covariance data at a measurement height of 6 m above the surface.

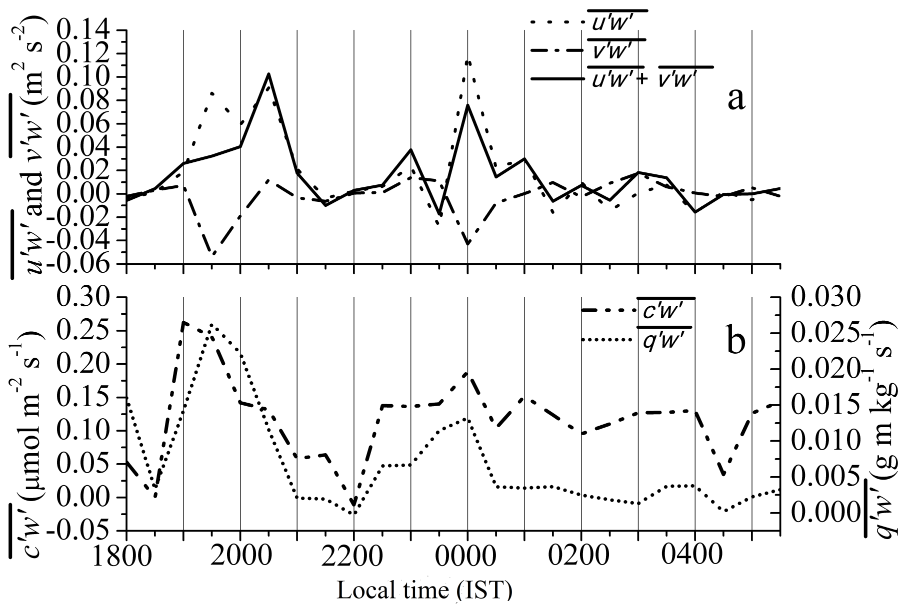

Fig. 10 Temporal variations of vertical kinematic fluxes of, (a) zonal and meridional momentum, and (b) water vapour and CO_2 calculated using the eddy-covariance data at a measurement height of 6 m above the surface.

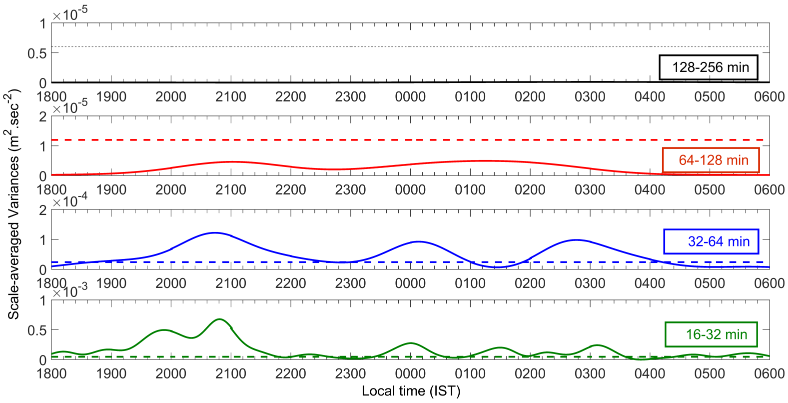

Fig. 11 Scale-averaged variances of vertical velocity (w) in different frequency bands. Time scales for the frequency bands are shown in the text boxes. Broken lines represent white noises for the corresponding frequency bands. The y-axis scale differs from panel to panel. Data are from the eddy-covariance measurement at 6 m.

The magnitude of the scale-averaged variance for the 'non-turbulent' eddies is statistically significant throughout the period of study (Fig. 14). It is higher than the corresponding white noise which is treated as the baseline for the comparison. However, the absolute value of the scale-averaged variance is three orders of magnitude smaller than the same for the 'turbulent' events.

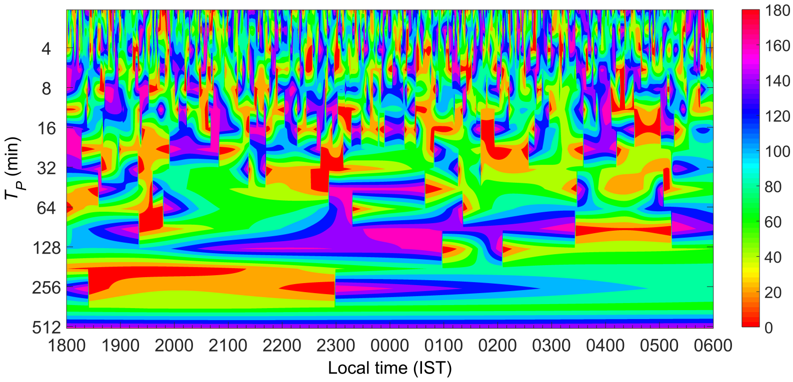

Fig. 12 Phase spectrum between vertical wind (w) and ambient air temperature (T) (ϕ_{wT} in $^\circ$) at 6 m. The x and y axes show the time of occurrence and the time period (T_P in min) of the oscillations, respectively. The scale on the y-axis is in reverse order. The colour bar shows the scale in degrees. Data are from the eddy-covariance measurement.

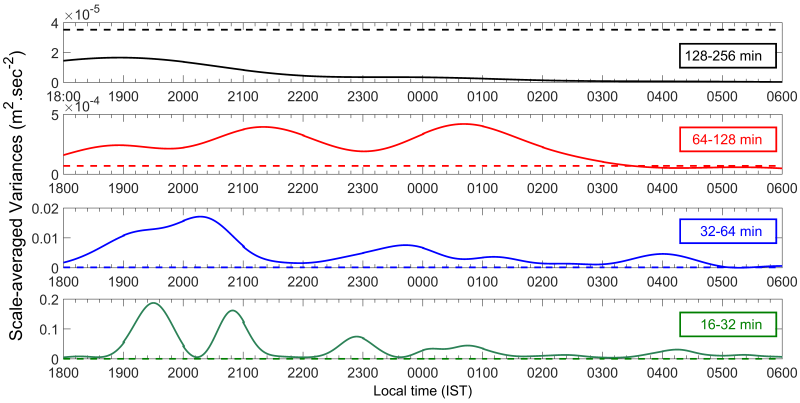

Fig. 13 Scale-averaged variances of horizontal wind speed (v_h) in different frequency bands. Time scales for the frequency bands are shown in the text boxes. Broken lines represent white noises for the corresponding frequency bands. The y-axis scale differs from panel to panel. Data are from the eddy-covariance measurement at 6 m.

Scale-averaged variance for the turbulent eddies becomes significant around 1930 IST and reaches a value of around 0.55 m^2 s^{-2}. The findings discussed earlier support the fact that the small-scale eddies become dominant during periods of intermittent turbulence. The evolution of the intermittency can be seen to happen around this time at the surface level. This observation suggests the intermittency of turbulence at the surface results from non-turbulent waves and instabilities that were present below the core of the LLJ.

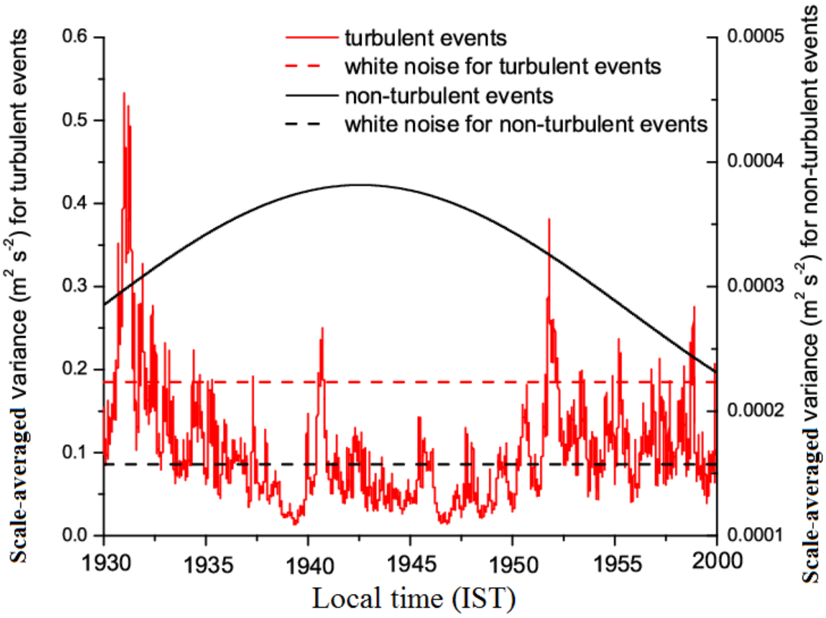

Fig. 14 Scale-averaged variances for turbulent and non-turbulent processes for one 30-minute period of vertical velocity (w) from the eddy-covariance data at 6 m above the surface.

5 Conclusions

We analyzed features of the nocturnal boundary layer during monsoon conditions over Peninsular India from collocated eddy-covariance, lidar and radiometer observations using wavelet and cospectral analysis. Such an analysis relating turbulence intermittency to the monsoon LLJ has not been conducted previously. Nocturnal, regional-scale jets were observed over the region and occurred in association with the large-scale monsoon flow. The genesis and propagation of turbulence in the presence of the LLJ were investigated, with the following key findings.

1. Large-scale oscillations of the wind velocity are present in the NBL as evidenced by the results of wavelet analysis.
2. The LLJ generates mechanical shear within the layers below the jet height, and is responsible for the genesis of sporadic turbulence within the stably-stratified surface layer.
3. The LLJ is associated with strong vertical shear in the horizontal velocity and strong updrafts and downdrafts occurred below the LLJ. These events introduce smaller periodic and turbulent fluctuations into the surface layer.
4. The large eddies contained below the jet transport a significant amount of TKE, analogous to the upside-down boundary layer described by Banta et al.

(2003).
5. Intermittent events observed at the surface occurred in association with the larger eddies generated by the LLJ. These events result in the enhancement of fluxes of heat, moisture, and CO_2 between the land surface and atmosphere.

Acknowledgements We extend our sincere gratitude to the Director of the Indian Institute of Tropical Meteorology (IITM) for all his constant encouragement and support. We also thank all the members of the CAIPEEX-IGOC team and the staff of the IITM-workshop for their assistance with this project. Data used in this manuscript can be obtained for research purpose by contacting the second author Dr. Thara V. Prabha. at thara@tropmet.res.in. CAIPEEX and the Centre for Climate Change Research (CCCR) are parts of IITM, an autonomous research institute of Ministry of Earth Sciences (MoES), Government of India. Wavelet software was provided by C. Torrence and G. Compo, and is available at URL: http://atoc.colorado.edu/research/wavelets/. Freely available Ferret program by NOAA's Pacific Marine Environmental Laboratory has been used for Fig. 1 in this paper (http://ferret.pmel.noaa.gov/Ferret/).

References

Acevedo OC, Fitzjarrald DR (2003) In the core of the night-effects of intermittent mixing on a horizontally heterogeneous surface. Boundary-Layer Meteorol 106:1–33

Ardanuy P (1979) On the observed diurnal oscillation of the Somali jet. Mon Weather Rev 107:1694–1700

Aubinet M, Vesala T, Papale D (2012) Eddy covariance: a practical guide to measurement and data analysis, Springer, the Netherlands, p 438

Banta RM (2008) Stable-boundary-layer regimes from the perspective of the low-level jet. Acta Geophys 56:58–87

Banta RM, Newsom R, Lundquist J, Pichugina Y, Coulter R, Mahrt L (2002) Nocturnal low-level jet characteristics over kansas during CASES-99. Boundary-Layer Meteorol 105:221–252

Banta RM, Pichugina YL, Newsom RK (2003) Relationship between low-level jet properties and turbulence kinetic energy in the nocturnal stable boundary layer. J Atmos Sci 60:2549–2555

Banta RM, Pichugina YL, Brewer WA (2006) Turbulent velocity-variance profiles in the stable boundary layer generated by a nocturnal low-level jet. J Atmos Sci 63:2700–2719

Banta RM, Mahrt L, Vickers D, Sun J, Balsley BB, Pichugina YL, Williams EJ (2007) The very stable boundary layer on nights with weak low-level jets. J Atmos Sci 64(9):3068–3090

Barthlott C, Drobinski P, Fesquet C, Dubos T, Pietras C (2007) Long-term study of coherent structures in the atmospheric surface layer. Boundary-Layer Meteorol 125(1):1–24

Berström H, Smedman AS (1995) Stably stratified flow in a marine atmospheric surface layer. Boundary-Layer Meteorol 72:239–265

Blackadar AK (1957) Boundary layer wind maxima and their significance for the growth of nocturnal inversions. Bull Amer Meteor Soc 38:283–290

Blumen W, Grossman R, Piper M (1999) Analysis of heat budget, dissipation and frontogenesis in a shallow density current. Boundary-Layer Meteorol 91:281–306

Bonin TA, Blumberg WG, Klein PM, Chilson PB (2015) Thermodynamic and turbulence characteristics of the southern great plains nocturnal boundary layer under differing turbulent regimes. Boundary-Layer Meteorol 157:401–420

Bunker AP (1965) Interaction of the Summer Monsoon Air with the Arabian Sea. Proc Symposium on Meteorological Results of the International Indian Ocean Expedition Bombay 22 July 1965:22–26

Chimonas G (1993) Surface drag instabilities in the atmospheric boundary layer. J Atmos Sci 50:1914–1924

Coulter RL, Doran J (2002) Spatial and temporal occurrences of intermittent turbulence during CASES-99. Boundary-Layer Meteorol 105:329–349

Cuxart J, Morales G, Terradellas E, Yagüe C (2002) Study of coherent structures and estimation of the pressure transport terms for the nocturnal stable boundary layer. Boundary-Layer Meteorol 105:305–328

Dee DP, Uppala S, Simmons A, Berrisford P, Poli P, Kobayashi S, Andrae U, Balmaseda M, Balsamo G, Bauer P, Bechtold P, Belijaars A, Berg L, Bidlot J, Bormann N, Delsol C, Dragani R, Fuentes M, Geer A, Haimberger L, Healy S, Hersbach H, Hólm E, Isaksen L, Källberg P, Köhler M, Matricardi M, McNally A, Monge-Sanz B, Morcrette J, Park B, Peubey C, Rosnay P, Tavolato C, Thépaut J, Vitart F (2011) The ERA-Interim reanalysis: Configuration and performance of the data assimilation system. Q J R Meteorol Soc 137(656):553–597

Duarte HF, Leclerc MY, Zhang G, Durden D, Kurzeja R, Parker M, Werth D (2015) Impact of nocturnal low-level jets on near-surface turbulence kinetic energy. Boundary-Layer Meteorol 156:349–370

Durden D, Nappo C, Leclerc M, Duarte H, Zhang G, Parker M, Kurzeja R (2013) On the impact of wave-like disturbances on turbulent fluxes and turbulence statistics in nighttime conditions: a case study. Biogeosci 10:8433–8443

Einaudi F, Bedard Jr A, Finnigan J (1989) A climatology of gravity waves and other coherent disturbances at the Boulder Atmospheric Observatory during March-April 1984. J Atmos Sci 46:303–329

Everson R, Sirovich L, Sreenivasan K (1990) Wavelet analysis of the turbulent jet. Phys Lett A 145:314–322

Farge M (1992) Wavelet transforms and their applications to turbulence. Ann Rev Fluid Mech 24:395–458

Findlater J (1969) A major low-level air current near the indian ocean during the northern summer. Q J R Meteorol Soc 95:362–380

Finnigan J (1988) Kinetic energy transfer between internal gravity waves and turbulence. J Atmos Sci 45:486–505

Frisch U, Sulem PL, Nelkin M (1978) A simple dynamical model of intermittent fully developed turbulence. J Fluid Mech 87(04):719–736

Fritts DC, Nappo C, Riggin DM, Balsley BB, Eichinger WE, Newsom RK (2003) Analysis of ducted motions in the stable nocturnal boundary layer during CASES-99. J Atmos Sci 60:2450–2472

Grossman RL, Durran DR (1984) Interaction of low-level flow with the western ghat mountains and offshore convection in the summer monsoon. Mon Weather Rev 112(4):652–672

Gu L, Falge EM, Boden T, Baldocchi DD, Black T, Saleska SR, Suni T, Verma SB, Vesala T, Wofsy SC, Xu L (2005) Objective threshold determination for nighttime eddy flux filtering. Agric For Meteorol 128(3):179–197

He P, Basu S (2015) Development of similarity relationships for energy dissipation rate and temperature structure parameter in stably stratified flows: a direct numerical simulation approach. Environ Fluid Mech 16:1–27

Hicks B, ODell D, Eash N, Sauer T (2015) Nocturnal intermittency in surface co_2 concentrations in sub-Saharan Africa. Agric For Meteorol 200:129–134

Howell J, Sun J (1999) Surface-layer fluxes in stable conditions. Boundary-Layer Meteorol 90:495–520

Hu XM, Klein PM, Xue M, Shapiro A, Nallapareddy A (2013) Enhanced vertical mixing associated with a nocturnal cold front passage and its impact on near-surface temperature and ozone concentration. J Geophys Res Atmos 118:2714–2728

Hudgins L, Friehe CA, Mayer ME (1993) Wavelet transforms and atmospheric turbulence. Phys Rev Lett 71:3279

Joseph P, Raman P (1966) Existence of low level westerly jet stream over peninsular India during july. Indian J Meteorol Geophys 17:407–410

Kaimal J, Finnigan J (1994) Atmospheric boundary layer Flows: their structure and measurement, Oxford Univ. Press, USA, p 289

Kalapureddy M, Rao D, Jain A, Ohno Y (2007) Wind profiler observations of a monsoon low-level jet over a tropical Indian station. Ann Geophys 25:2125–2137

Karipot A, Leclerc M, Zhang G, Martin T, Starr G, Hollinger D, McCaughey J, Hendrey G (2006) Nocturnal CO_2 exchange over a tall forest canopy associated with intermittent low-level jet activity. Theor Appl Climatol 85:243–248

Karipot A, Leclerc MY, Zhang G, Lewin KF, Nagy J, Hendrey GR, Starr G (2008) Influence of nocturnal low-level jet on turbulence structure and CO_2 flux measurements over a forest canopy. J Geophys Res Atmos 113

Karipot A, Leclerc MY, Zhang G (2009) Characteristics of nocturnal low-level jets observed in the north Florida area. Mon Weather Rev 137:2605–2621

Katul GG, Albertson J, Parlange M, Chu CR, Stricker H (1994) Conditional sampling, bursting, and the intermittent structure of sensible heat flux.

J Geophys Res Atmos 99:22,869–22,876

Krishnamurti TN, Molinari J, Pan HL (1976) Numerical simulation of the Somali jet. J Atmos Sci 33:2350–2362

Kulkarni J, Maheskumar R, Morwal S, Padma Kumari B, Konwar M, Deshpande C, Joshi R, Bhalwankar R, Pandithurai G, Safai P, Narkhedkar S, Dani K, Nath A, Nair S, Sapre V, Puranik P, Kandalgaonkar S, Mujumdar V, Khaladkar R, Vijayakumar R, Prabha T, Goswami B (2012) The cloud aerosol interaction and precipitation enhancement experiment (CAIPEEX): overview and preliminary results. Curr Sci 102:413–425

Lau K, Weng H (1995) Climate signal detection using wavelet transform: How to make a time series sing. Bull Am Meteor Soc 76:2391–2402

Lee X, Black TA, den Hartog G, Neumann HH, Nesic Z, Olejnik J (1996) Carbon dioxide exchange and nocturnal processes over a mixed deciduous forest. Agric For Meteorol 81:13–29

Mahrt L (1985) Vertical structure and turbulence in the very stable boundary layer. J Atmos Sci 42:2333–2349

Mahrt L (1998) Nocturnal boundary-layer regimes. Boundary-Layer Meteorol 88:255–278

Mahrt L (1999) Stratified atmospheric boundary layers. Boundary-Layer Meteorol 90:375–396

Mahrt L (2010) Common microfronts and other solitary events in the nocturnal boundary layer. Q J R Meteorol Soc 136:1712–1722

Mahrt L (2014) Stably stratified atmospheric boundary layers. Ann Rev Fluid Mech 46:23–45

Mahrt L, Vickers D (2002) Contrasting vertical structures of nocturnal boundary layers. Boundary-Layer Meteorol 105:351–363

Malhi YS (1995) The significance of the dual solutions for heat fluxes measured by the temperature fluctuation method in stable conditions. Boundary-Layer Meteorol 74:389–396

Meillier Y, Frehlich R, Jones R, Balsley B (2008) Modulation of small-scale turbulence by ducted gravity waves in the nocturnal boundary layer. J Atmos Sci 65:1414–1427

Nair SK, Prabha TV, Purushothaman N, Sijikumar S, Muralidharan S, Kirankumar N, Subrahamanyam D, Anurose T, Prijith S, Namboodiri K (2014) Diurnal variations of the low-level jet over peninsular India during the onset of Asian summer monsoon. Theor Appl Climatol 120:1–12

Nappo C, Miller D, Hiscox A (2008) Wave-modified flux and plume dispersion in the stable boundary layer. Boundary-Layer Meteorol 129:211–223

Nappo CJ (1991) Sporadic breakdowns of stability in the PBL over simple and complex terrain. Boundary-Layer Meteorol 54:69–87

Nappo CJ (2012) An introduction to atmospheric gravity waves, vol 102, Academic Press, USA, p 276

Newsom RK, Banta RM (2003) Shear-flow instability in the stable nocturnal boundary layer as observed by doppler lidar during CASES-99. J Atmos Sci 60:16–33

Ohya Y, Neff DE, Meroney RN (1997) Turbulence structure in a strati-

fied boundary layer under stable conditions. Boundary-Layer Meteorol 83:139–162
Pichugina YL, Banta RM (2010) Stable boundary layer depth from high-resolution measurements of the mean wind profile. J Appl Meteorol Climatol 49(1):20–35
Poulos GS, Blumen W, Fritts DC, Lundquist JK, Sun J, Burns SP, Nappo C, Banta R, Newsom R, Cuxart J, Terradellas E, Balsley B, Jensen M (2002) CASES-99: A comprehensive investigation of the stable nocturnal boundary layer. Bull Am Meteor Soc 83(4):555–581
Prabha TV, Leclerc MY, Karipot A, Hollinger DY (2007) Low-frequency effects on eddy covariance fluxes under the influence of a low-level jet. J Appl Meteorol Climatol 46(3):338–352
Prabha TV, Leclerc MY, Karipot A, Hollinger DY, Mursch-Radlgruber E (2008) Influence of nocturnal low-level jets on eddy-covariance fluxes over a tall forest canopy. Boundary-Layer Meteorol 126:219–236
Prabha TV, Khain A, Maheshkumar R, Pandithurai G, Kulkarni J, Konwar M, Goswami B (2011) Microphysics of premonsoon and monsoon clouds as seen from in situ measurements during the cloud aerosol interaction and precipitation enhancement experiment (CAIPEEX). J Atmos Sci 68:1882–1901
Qiu J, Shaw RH, et al. (1995) Pseudo-wavelet analysis of turbulence patterns in three vegetation layers. Boundary-Layer Meteorol 72:177–204
Román-Cascón C, Yagüe C, Mahrt L, Sastre M, Steeneveld GJ, Pardyjak E, Boer A, Hartogensis O (2015) Interactions among drainage flows, gravity waves and turbulence: a BLLAST case study. Atmos Chem Phys 15:9031–9047
Rorai C, Mininni P, Pouquet A (2014) Turbulence comes in bursts in stably stratified flows. Physl Rev E 89:043,002
Ruchith R, Raj PE, Kalapureddy M, Deshpande SM, Dani K (2014) Time evolution of monsoon low-level jet observed over an indian tropical station during the peak monsoon period from high-resolution doppler wind lidar measurements. J Geophys Res Atmos 119:1786–1795
Salmond J, Oke T, Grimmond C, Roberts S, Offerle B (2005) Venting of heat and carbon dioxide from urban canyons at night. J Appl Meteorol 44:1180–1194
Salmond JA (2005) Wavelet analysis of intermittent turbulence in a very stable nocturnal boundary layer: implications for the vertical mixing of ozone. Boundary-Layer Meteorol 114:463–488
Sivaramakrishnan S, Saxena S, Vernekar K (1992) Characteristics of turbulent fluxes of sensible heat and momentum in the surface boundary layer during the indian summer monsoon. Boundary-Layer Meteorol 60:95–108
Smedman AS, Tjernström M, Högström U (1993) Analysis of the turbulence structure of a marine low-level jet. Boundary-Layer Meteorol 66:105–126
Sorbjan Z, Czerwinska A (2013) Statistics of turbulence in the stable boundary layer affected by gravity waves. Boundary-Layer Meteorol 148:73–91

Stull RB (1988) An introduction to boundary layer meteorology, vol 13, Springer, the Netherlands

Sun J (2011) Vertical variations of mixing lengths under neutral and stable conditions during CASES-99. J Appl Meteorol Climatol 50:2030–2041

Sun J, Burns SP, Lenschow DH, Banta R, Newsom R, Coulter R, Frasier S, Ince T, Nappo C, Cuxart J, Blumen W, Lee X, Hu XZ (2002) Intermittent turbulence associated with a density current passage in the stable boundary layer. Boundary-Layer Meteorol 105:199–219

Sun J, Lenschow DH, Burns SP, Banta RM, Newsom RK, Coulter R, Frasier S, Ince T, Nappo C, Balsley BB, et al. (2004) Atmospheric disturbances that generate intermittent turbulence in nocturnal boundary layers. Boundary-Layer Meteorol 110(2):255–279

Sun J, Lenschow DH, LeMone MA, Mahrt L (2016) The role of large-coherent-eddy transport in the atmospheric surface layer based on CASES-99 observations. Boundary-Layer Meteorol 160:83–111

Terradellas E, Soler M, Ferreres E, Bravo M (2005) Analysis of oscillations in the stable atmospheric boundary layer using wavelet methods. Boundary-Layer Meteorol 114:489–518

Thomas C, Foken T (2005) Detection of long-term coherent exchange over spruce forest using wavelet analysis. Theor Appl Climatol 80(2):91–104

Torrence C, Compo GP (1998) A practical guide to wavelet analysis. Bull Am Meteor Soc 79:61–78

Viana S, Yagüe C, Maqueda G (2009) Propagation and effects of a mesoscale gravity wave over a weakly-stratified nocturnal boundary layer during the SABLES2006 field campaign. Boundary-Layer Meteorol 133:165–188

Vickers D, Mahrt L (1997) Quality control and flux sampling problems for tower and aircraft data. J Atm Oc Tech 14:512–526

Wang Y, Creegan E, Felton M, Ligon D, Huynh G (2013) Investigation of nocturnal low-level jet–generated gravity waves over Oklahoma City during morning boundary layer transition period using doppler wind lidar data. J Appl Remote Sens 7:073,487–073,487

Woods BK, Smith RB (2010) Energy flux and wavelet diagnostics of secondary mountain waves. J Atmos Sci 67:3721–3738

Wu X, Zhang J (2008a) Instability of a stratified boundary layer and its coupling with internal gravity waves. Part 1. linear and nonlinear instabilities. J Fluid Mech 595:379–408

Wu X, Zhang J (2008b) Instability of a stratified boundary layer and its coupling with internal gravity waves. Part 2. coupling with internal gravity waves via topography. J Fluid Mech 595:409–433

Wyngaard JC (2010) Turbulence in the Atmosphere, vol 774, Cambridge University Press, USA

Xue M, Xu Q, Droegemeier KK (1997) A theoretical and numerical study of density currents in nonconstant shear flows. J Atmos Sci 54:1998–2019

Zeri M, Sá LD (2011) Horizontal and vertical turbulent fluxes forced by a gravity wave event in the nocturnal atmospheric surface layer over the Amazon forest. Boundary-layer Meteorol 138:413–431

Zhou B, Chow FK (2014) Nested large-eddy simulations of the intermittently turbulent stable atmospheric boundary layer over real terrain. J Atmos Sci 71:1021–1039

Zilitinkevich S, Elperin T, Kleeorin N, Lvov V, Rogachevskii I (2009) Energy-and flux-budget turbulence closure model for stably stratified flows. Part II: the role of internal gravity waves. Boundary-Layer Meteorol 133:139–164